Unraveling the Teleconnection Mechanisms that Induce Wintertime Temperature Anomalies over the Northern Hemisphere Continents in Response to the MJO

KYONG-HWAN SEO AND HYUN-JU LEE

Division of Earth Environmental System, Department of Atmospheric Sciences, Pusan National University, Busan, South Korea

DARGAN M. W. FRIERSON

Department of Atmospheric Sciences, University of Washington, Seattle, Washington

(Manuscript received 21 January 2016, in final form 30 May 2016)

ABSTRACT

Significant extratropical surface air temperature variations arise as a result of teleconnections induced by the Madden–Julian oscillation (MJO). The authors elucidate the detailed physical processes responsible for the development of temperature anomalies over Northern Hemisphere continents in response to MJO-induced heating using an intraseasonal perturbation thermodynamic equation and a wave activity tracing technique. A quantitative assessment demonstrates that surface air temperature variations are due to dynamical processes associated with a meridionally propagating Rossby wave train. Over East Asia, a local Hadley circulation causes adiabatic subsidence following MJO phase 3 to be a main driver for the warming. Meanwhile, for North America and eastern Europe, horizontal temperature advection by northerlies or southerlies is the key process for warming or cooling. A ray-tracing analysis illustrates that Rossby waves with zonal wavenumbers 2 and 3 influence the surface warming over North America and a faster wavenumber 4 affects surface temperature over eastern Europe. Although recent studies demonstrate the impacts of the Arctic Oscillation, Arctic sea ice melting, and Eurasian snow cover variations on extremely cold wintertime episodes over the NH extratropics, the weather and climate there are still considerably modulated through teleconnections induced by the tropical heat forcing. In addition, the authors show that the MJO is a real source of predictability for strong warm/cold events over these continents, suggesting a higher possibility of making a skillful forecast of temperature extremes with over 1 month of lead time.

1. Introduction

The Madden–Julian oscillation (MJO) is the most prominent physical mode over the tropics in the intraseasonal band with a characteristic time scale of 30–70 days (Madden and Julian 1972). Previous studies have shown that the tropical heating associated with the MJO induces atmospheric circulation anomalies in both the tropics and midlatitudes, through equatorially trapped Kelvin and Rossby waves and an extratropical Rossby wave train, respectively (e.g., Matthews et al. 2004; Seo and Son 2012; Adames and Wallace 2014). The MJO influences a variety of atmospheric and oceanic phenomena, including tropical cyclones (e.g., Liebmann et al. 1994; Sobel and Maloney 2000; Hall et al. 2001; Bessafi and Wheeler 2006; Ho et al. 2006), the Asian summer monsoon (e.g., Yasunari 1979; Hoyos and Webster 2007; Seo et al. 2007), the Australian–Indonesian monsoon (Hendon and Liebmann 1990; Wheeler and McBride 2005), the African monsoon (Maloney and Shaman 2008), El Niño (Zavala-Garay et al. 2005; McPhaden 1999), the Pacific–North America pattern, Arctic Oscillation or North Atlantic Oscillation (e.g., Zhou and Miller 2005; Cassou 2008; L'Heureux and Higgins 2008; Lin et al. 2009; Riddle et al. 2013), the jet streams (e.g., Matthews et al. 2004; Seo and Son 2012), and pineapple express or atmospheric river events (e.g., Kerr 2006). Recently, Yoo et al. (2012a) demonstrated that MJO-induced Rossby wave propagation contributes to Arctic air temperature amplification typically associated with the response to global warming (Yoo et al. 2012b).

Corresponding author address: Dr. Kyong-Hwan Seo, Department of Atmospheric Sciences, Pusan National University, Jangjeon-dong, Busan 609735, South Korea.
E-mail: khseo@pusan.ac.kr

DOI: 10.1175/JAS-D-16-0036.1

Since these weather and climate phenomena cause a great deal of societal and economic impacts, the MJO is considered to be the most important tropical variability on a time scale less than a season.

The dynamical mechanisms of the circulation response to the MJO heating have been investigated by Seo and Son (2012). In their study, tropical circulation anomalies are a result of the interaction between equatorial Kelvin and Rossby waves, whereas extratropical stationary waves are shown to be excited by horizontal divergence of the upper-level perturbation flow. A ray-tracing analysis using nondivergent barotropic vorticity theory indicates that Rossby wave activity arises from the meridional propagation of zonal wavenumbers 2 and 3 in the Northern Hemisphere during boreal winter. Accordingly, significant upper- and lower-level circulation anomalies appear in remote areas including Eurasia and North America. Therefore, it is expected that the MJO would affect air temperature over these continents as well.

Previous studies have in fact demonstrated intraseasonal modulation of surface air temperature over East Asia, eastern North America, Alaska, and the Arctic region during northern winter by the MJO cycle (Vecchi and Bond 2004; Jeong et al. 2005; Lin and Brunet 2009; Yoo et al. 2012a; Riddle et al. 2013; Oliver 2015). For example, a significant cooling signal arises over Alaska and the Arctic when enhanced convection is located over the Maritime Continent [i.e., MJO phase 5 defined in Wheeler and Hendon (2004)] or equivalently about 15 days after suppressed convection is located over the Maritime Continent (i.e., MJO phase 1) (Vecchi and Bond 2004; Zhou et al. 2011; Yoo et al. 2012a; Oliver 2015). Cold surges occur over East Asia when convection is located over the tropical Indian Ocean (i.e., MJO phase 3) (Jeong et al. 2005). A snowstorm event took place over the eastern United States during the 2009/10 winter season during phases 8, 1, and 2 of the MJO (Moon et al. 2012). A warming signal appears over eastern North America ~2 pentads later following MJO phase 2 when enhanced convection is located over the central Indian Ocean (Lin and Brunet 2009; Riddle et al. 2013). All these studies speculate that the warming and cooling events are caused by both advection of air temperature and variations in downward longwave radiation from changes in specific humidity, set up by Rossby wave propagation from the tropical Indian or Pacific Ocean to the extratropics. However, the detailed mechanisms and their relative importance have not been established. Furthermore, an explicit validation using barotropic Rossby wave theory and wave energy tracing has not been performed.

In this study, the physical processes responsible for variations in surface air temperature over the Northern Hemisphere continents in response to the MJO are examined through an intraseasonal thermodynamic equation. By evaluating the relative importance of terms such as horizontal temperature advection, adiabatic heating, and diabatic heating, we present the dominant physical processes of MJO-induced surface air temperature variation over three major Northern Hemisphere regions: East Asia, North America, and eastern Europe. Furthermore, we explicitly show that a local overturning circulation induced by the tropical forcing is directly related to the changes in surface temperature over East Asia and the Rossby wave propagation plays a role over North America and eastern Europe.

In addition, we demonstrate the occurrence rate of extreme warm/cold events for strong MJO cases. The information gained from this study can be useful for improving the skill of long-term temperature prediction. We show here that the MJO is a predictability source on the intraseasonal time scale for the forecast of strong warm/cold events over these continents.

2. Data and methodology

As a proxy of deep convection, we use Advanced Very High Resolution Radiometer (AVHRR) daily mean outgoing longwave radiation (OLR) data obtained from the National Oceanic and Atmospheric Administration (NOAA) for the period 1979–2010. In this study, only the boreal winter season [December–February (DJF)] is considered. For dynamic and thermodynamic variables, the ERA-Interim dataset is used. To determine extreme surface air temperature events, we utilize the Hadley Centre Global Historical Climatology Network (GHCN)-Daily (HadGHCND) station data with a resolution of 3.75° × 2.5°.

To extract intraseasonal variability, we eliminate seasonal variation by removing the first three harmonics of the annual cycle from the data and bandpass filter (20–90 day) the resulting anomalies using a Lanczos filter. After performing an empirical orthogonal function (EOF) analysis on the intraseasonally filtered OLR anomaly and obtaining the resultant two leading EOF patterns, we construct eight different phases (Wheeler and Hendon 2004) that represent the typical evolution of the MJO. For example, enhanced convection located over the Indian Ocean during phases 2 and 3, over the Maritime Continent during phases 4 and 5, over the western Pacific during phases 6 and 7, and over the Western Hemisphere and Africa during phases 8 and 1. Composite fields are constructed for strong MJO events where the PC amplitude (i.e., $\sqrt{\mathrm{PC1}^2 + \mathrm{PC2}^2}$) is greater than 1.5 for each MJO phase. For the statistical significance of the composites, a Monte Carlo test is performed with 500 random resamplings of the data to compute the null probability distribution.

To perform intraseasonal temperature diagnostics, we begin with the thermodynamic equation as shown below:

$$\frac{\partial T}{\partial t} = -\mathbf{V}_H \cdot \nabla_H T + S_P \omega + Q + \mathrm{Res}, \qquad (1)$$

where T is the temperature, $\mathbf{V}_\mathrm{H}$ is the horizontal velocity, and ω is the vertical velocity in pressure coordinates. The stability parameter S_P is expressed as $S_P = (R/C_P)(T/P) - (\partial T/\partial p)$, where R is the gas constant for dry air and C_p is the specific heat of dry air at constant pressure, and Q is the diabatic heating estimated from the apparent heat source of Yanai et al. (1973). The first term on the right-hand side of Eq. (1) represents temperature advection by the horizontal wind. The second and third terms denote, respectively, adiabatic and diabatic heating. A residual term contains diffusion effects and numerical error.

To drive the intraseasonal perturbation thermodynamic equation, the variables are divided into mean and anomaly fields, and the latter is further decomposed into MJO and non-MJO components,

$$A = \overline{A} + A' \quad \text{and} \quad A' = \{A\} + A^*, \qquad (2)$$

where the overbar denotes the DJF mean and the prime is the total anomaly. Curly brackets and the asterisk represent the MJO and non-MJO components, respectively. The MJO component was extracted using a bandpass filter and the non-MJO component was calculated as the difference between the total anomaly and the MJO component. Using Eq. (2), the intraseasonal perturbation thermodynamic equation takes the following form:

$$\begin{aligned}\frac{\partial\{T\}}{\partial t} &= -\overline{\mathbf{V}_H} \cdot \nabla_H\{T\} - \{\mathbf{V}_H\} \cdot \nabla_H \overline{T} - \{\mathbf{V}'_H \cdot \nabla_H T'\} \\ &\quad + \left(\frac{R}{C_P}\frac{\{T\}}{P} - \frac{\partial\{T\}}{\partial p}\right)\overline{\omega} + \left(\frac{R}{C_P}\frac{\overline{T}}{P} - \frac{\partial\overline{T}}{\partial p}\right)\{\omega\} \\ &\quad + \left(\left\{\frac{R}{C_P}\frac{T'}{P}\omega'\right\} - \left\{\frac{\partial T'}{\partial p}\omega'\right\}\right) + \{Q_{\mathrm{Dia}}\} + \{\mathrm{Res}\}.\end{aligned} \qquad (3)$$

The left-hand term is the MJO temperature tendency term. The first three terms on the right-hand side of the equation are related to horizontal temperature advection, representing MJO temperature advection by the time-mean wind, the advection of time-mean temperature by the MJO horizontal wind, and the interaction between anomalies. The next three terms are adiabatic heating and correspond to the interaction between the MJO temperature and the time-mean vertical wind, the time-mean temperature and the MJO vertical wind, and the interaction between the two anomalies. The seventh term denotes the intraseasonal part of the diabatic heating. The calculation of each term can reveal the dominant physical processes causing temperature anomalies. The residual term is extremely small so it is neglected (not shown).

The circulation response to MJO forcing requires time for Rossby waves to propagate meridionally, so the circulation anomaly formed by the MJO in the midlatitudes is the lagged response (i.e., Matthews et al. 2004; Cassou 2008; Yoo et al. 2012a). To incorporate this fact, we integrate the individual terms in Eq. (3) from day 0 to lag t days for each MJO phase. To examine the net effect of the MJO at any phase onward, the lag-0-day field is assumed to be zero. The computation is performed by applying the following relation:

$$\int_{\mathrm{lag}=0}^{\mathrm{lag}=t} \frac{\partial A}{\partial t}\, dt = A(t), \qquad (4)$$

where $\partial A/\partial t$ is any term in Eq. (3). The resulting term has units of temperature (K) so that this transformation facilitates the interpretation of each term in this delayed and accumulated response to the MJO.

For Rossby wave energy propagation tracing, the nondivergent barotropic Rossby wave theory of Hoskins and Karoly (1981) and Hoskins and Ambrizzi (1993) is applied. The dispersion relationship for the barotropic Rossby wave on a beta plane is expressed as $\omega = \overline{U}k - \beta_* k/K^2$, where ω is frequency; $\overline{U}$ is a basic-state zonal flow; the square of the total wavenumber is $K^2 = k^2 + l^2$ with zonal and meridional wavenumbers of k and l, respectively; and $\beta_* = \partial f/\partial y - \partial^2\overline{U}/\partial y^2$. The above dispersion relation provides meridional wavenumbers for a specified zonal wavenumber k in stationary waves ($\omega = 0$); then the group velocities for the zonal and meridional directions can be estimated using $c_{gx} = \partial\omega/\partial k = \overline{U} + \beta_*(k^2 - l^2)/K^4 = c + 2\beta_* k^2/K^4$ and $c_{gy} = \partial\omega/\partial l = 2\beta_* kl/K^4$. These group velocities can be converted to the ray of the wave activity by solving the following simple relations: $dx/dt = c_{gx}$ and $dy/dt = c_{gy}$. The location of the ray is calculated by using the fourth-order Runge–Kutta method (Press et al. 1992; Seo and Son 2012).

3. Results

a. Northern Hemisphere temperature anomalies

The surface air temperature fields for the canonical eight phases of the MJO demonstrate several peculiar warm and cold anomaly regions—for example, over

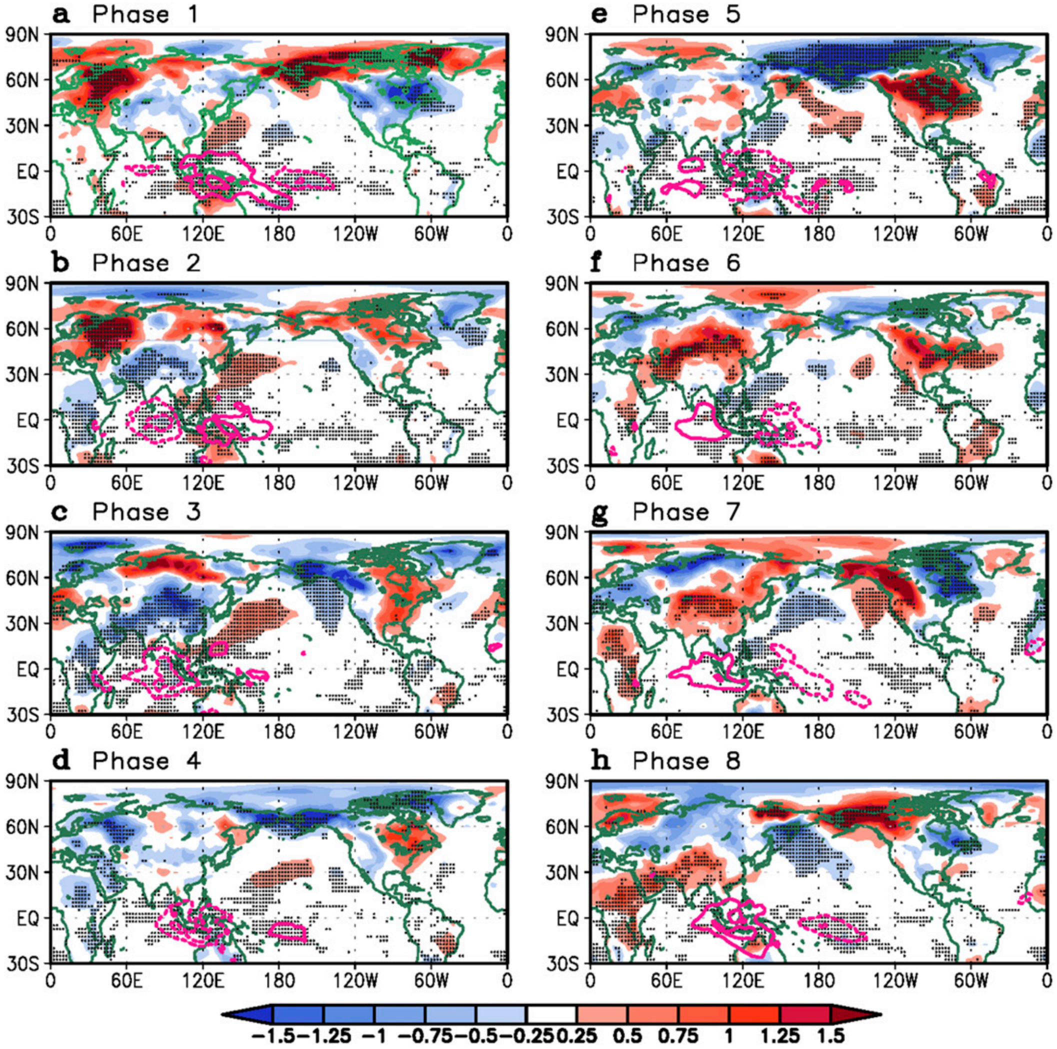

FIG. 1. Wintertime convection and surface temperature anomaly composites for the eight phases of the MJO. Composites of intraseasonally filtered OLR (magenta contours; interval of 15 W m^{-2}) and 2-m air temperature (shading; interval of 0.25 K) anomalies for each MJO phase. Dots indicate statistically significant temperature anomaly regions at the 95% confidence level.

East Asia, North America, the Arctic Sea, and Europe (Fig. 1). Arctic amplification of surface air temperature has been investigated in Yoo et al. (2012a,b) and poleward-propagating Rossby waves enhanced by localized MJO forcing have been found to be responsible for the formation of the warm anomalies there. During phase 3 (in Fig. 1c), when enhanced convection is located over the central Indian Ocean, cold anomalies appear over East Asia (EA) and the reverse appears during phases 6 and 7 (Figs. 1f,g, when enhanced convection is located over the western Pacific). In addition, a significant warm anomaly is seen over North America (NA) during phase 5, whereas cold anomalies appear there during phase 1 (Figs. 1a and 1e). More significant warm (cold) anomaly centers appear over eastern Europe (EE) during phases 1 and 2 (4). In this study, only these three midlatitude continental regions that show prominent temperature anomalies are focused, and over these regions, MJO-related temperature anomaly accounts for approximately 30% of total temperature anomaly variation in the three domains during wintertime (through a calculation of variance ratio).

As shown in Seo and Son (2012), the anomalies in midlatitudes are related to Rossby wave propagation from the tropics. It usually takes about 2–3 weeks to reach the northern continents and fully develop there (Jin and Hoskins 1995). Therefore, we can conjecture that the anomalous warm and cold anomalies seen over the continents are actually a lagged and accumulated response to the tropical forcing over the preceding

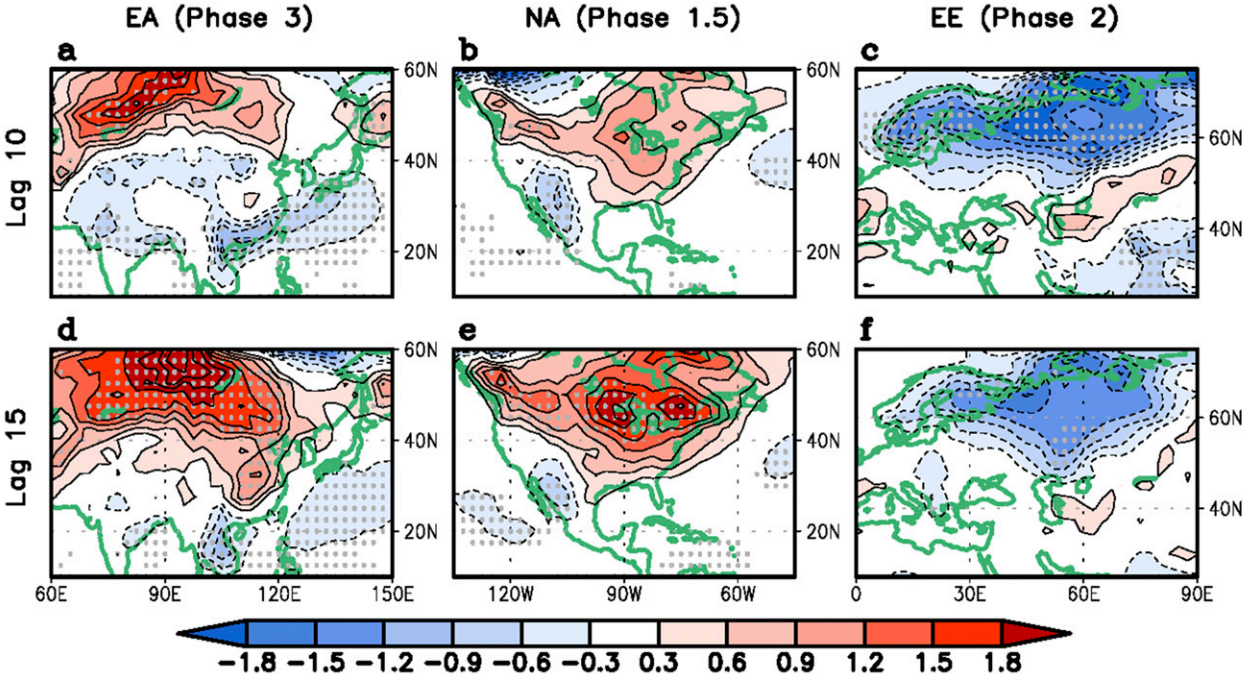

FIG. 2. MJO-induced surface air temperature variation over three continents. (left) Wintertime lagged composites of intraseasonally filtered 2-m air temperature anomaly (shading; interval of 0.3 K) at days (a) 10 and (d) 15 after the initial MJO phase 3 for EA. (center), (right) As in (a),(d), except lagged from (b),(e) an initial MJO phase 1.5 for NA and (c),(f) an initial MJO phase 2 for EE. A Monte Carlo test is performed by using 500 random samples and the gray dotted area represents significant regions at the 95% confidence level.

1–3 weeks (e.g., Cassou 2008). Considering that the time interval between two MJO phases is about 5–7 days, warm anomalies over EA are developed initially around phase 3, while warm anomalies over NA begin at around phase 1 or 2 (Fig. 2). For EE, cold anomalies begin to develop when enhanced convective heating is located over the central Indian Ocean (i.e., phase 2; the red dotted line in Fig. 1b) and suppressed convection is over the Maritime Continent and the far western Pacific. For the sake of easy comparison, phases 1.5, 2, and 3 are selected for the two warm and one cold anomaly cases since deep convection is located near the central Indian Ocean for these phases. The results for the opposite cases (i.e., at phase 7 for EA, at phase 5.5 for NA, and at phase 6 for EE) are almost identical with a sign reversal (not shown). Note that phase 1.5 (5.5) is a 45° segment centered on the diagonal line in the third (first) quadrant in a phase diagram.

Using Eqs. (3) and (4), we show time–height lagged composites for each of the individual terms to investigate dominant physical processes. The selected area is 25°–55°N, 60°–120°E for EA, 100°–60°W, 35°–60°N for NA, and 50°–70°N, 30°–75°E for EE.

b. *The East Asian teleconnection*

Left panels of Fig. 3 show the temporal evolution of the integrated field for each thermodynamic term over EA starting at phase 3. The tendency term (Fig. 3a) indicates a gradual increase of temperature anomalies with a peak of ~2.0 K appearing at the surface between days 15 and 20. The dynamic term (Fig. 3b), calculated as a sum of the horizontal advection (Fig. 3c) and adiabatic vertical advection (Fig. 3d), has a pronounced similarity with the tendency term. The diabatic term (Fig. 3e), calculated from the large-scale thermodynamic budget, show an opposite effect to the adiabatic term throughout the troposphere with a weak cooling signal at the surface. Adiabatic subsidence induces a very strong warm anomaly throughout the troposphere with a peak in the upper troposphere (Fig. 3d). Among the adiabatic components, vertical advection of the basic-state temperature field by the MJO-induced vertical velocity is clearly the strongest as shown in Fig. 4. Examining the time evolution of the vertical structure of the MJO-induced adiabatic vertical motion (see Fig. 5b) demonstrates that the warm anomaly develops at 200 hPa along 30°N by day 5 (not shown) as a result of sinking motions, and during days 10–15 significant downward motion near the surface and a resulting adiabatic warming are seen (Fig. 5b). Therefore, the warming over EA is associated with significant adiabatic subsidence over EA forced by MJO-related tropical convection. This direct circulation can be interpreted as

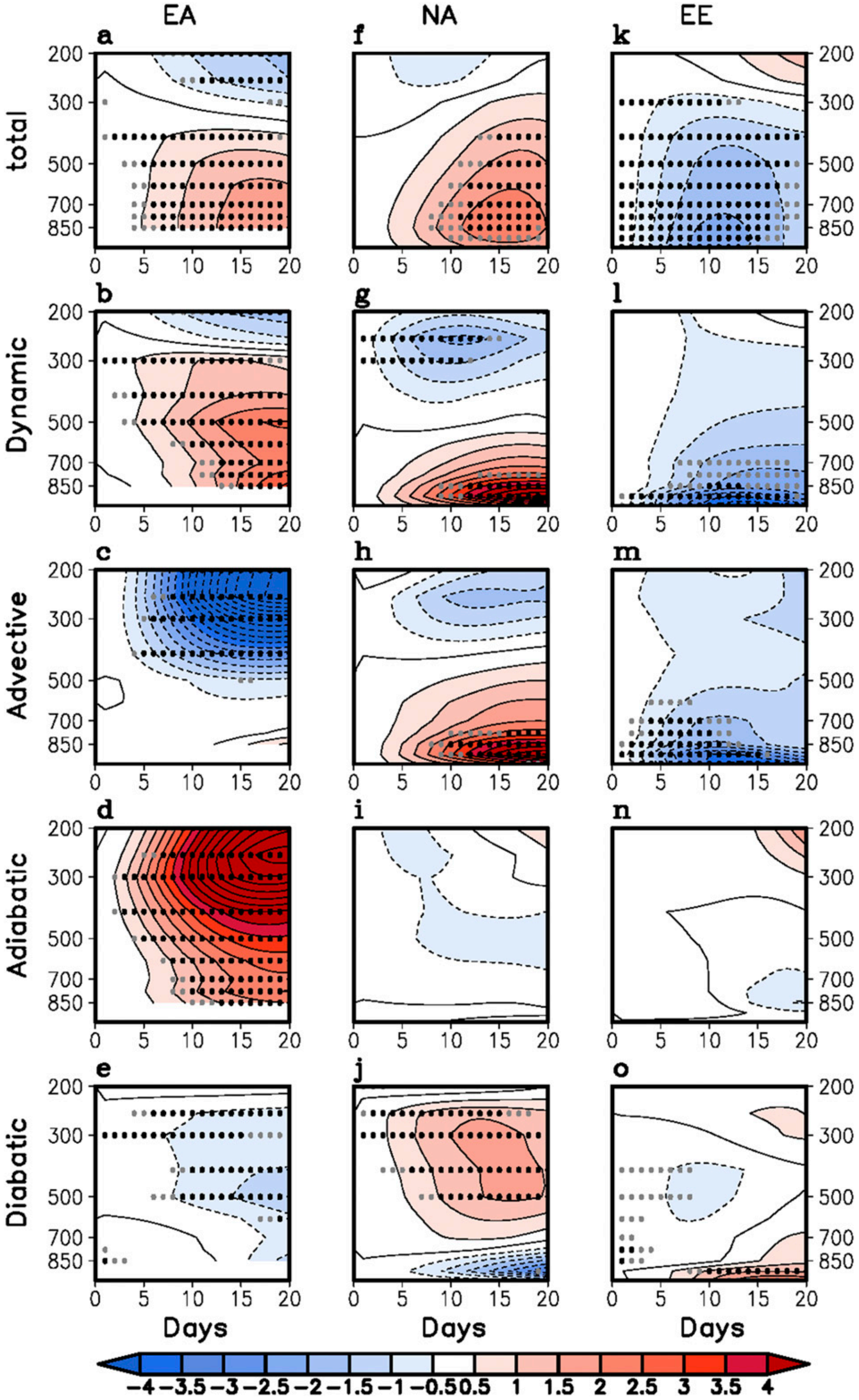

FIG. 3. Time evolution of integrated thermodynamic equation terms. Time–height cross section of the lagged composite of the MJO-induced air temperature integrated for the initial MJO (a)–(e) phase 3 for EA, (f)–(j) phase 1.5 for NA, and (k)–(o) phase 2 for EE. Integrated temperature fields (top to bottom) from the tendency term, dynamic (advective + adiabatic) term, horizontal advective term, adiabatic vertical motion term, and diabatic term. All variables are averaged over 25°–55°N, 60°–120°E for EA, 35°–60°N, 100°–60°W for NA, and 50°–70°N, 30°–75°E for EE. Air temperature fields below the surface are not plotted. The contour interval is 0.5 K. The gray and black dots represent statistically significant areas at the 90% and 95% confidence levels, respectively.

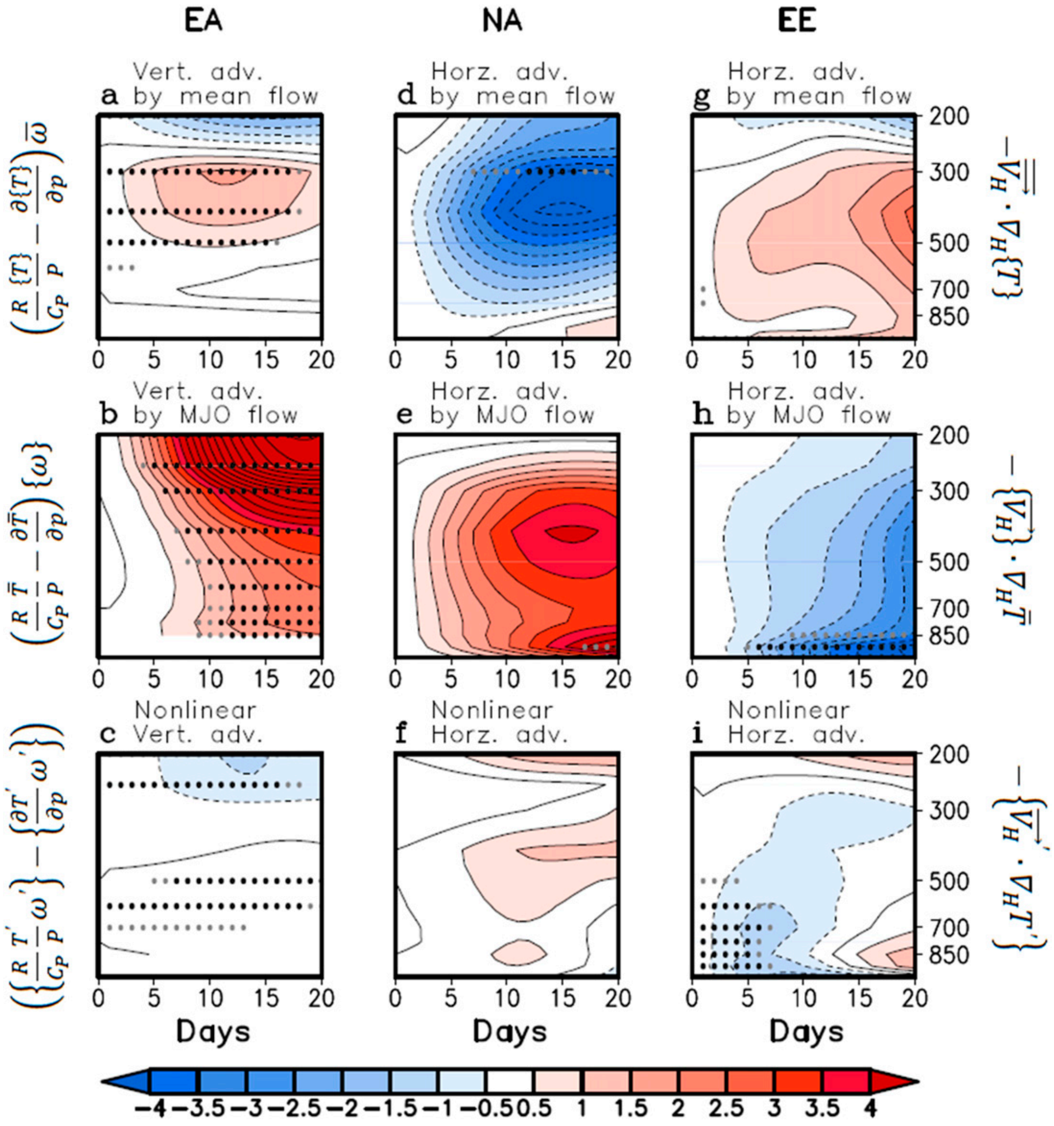

FIG. 4. Time evolution of integrated temperature terms representing adiabatic vertical motion and horizontal advection. Time–height cross section of the lagged composite of the MJO-related air temperature integrated for initial MJO (a)–(c) phase 3 for EA, (d)–(f) phase 1.5 for NA, and (g)–(i) phase 2 for EE. (left) Integrated temperature fields from (a) the vertical advection of MJO temperature by the time-mean vertical flow, (b) the vertical advection of time-mean temperature by the MJO vertical flow, and (c) the nonlinear vertical advection of MJO temperature by the MJO vertical flow. (center),(right) Integrated temperature fields from (d),(g) the horizontal advection of MJO temperature by the time-mean horizontal flow, (e),(h) the horizontal advection of time-mean temperature by the MJO horizontal flow, and (f),(i) the nonlinear horizontal advection of MJO temperature by the MJO horizontal flow. The contour interval in all plots is 0.5 K.

a local Hadley cell characterized by tropical upward motion forced by convective heating and downward motion with accompanying adiabatic warming over the subtropics.

By contrast, horizontal advection causes a cooling tendency in the middle and upper troposphere (Fig. 3c). At the surface, horizontal advection gives rise to only a slight warming after day 15. So the major contribution to the surface warm anomaly over EA comes almost solely from adiabatic subsidence due to MJO-induced vertical wind anomalies. The time evolution of the surface air temperature over EA (Fig. 6a) confirms this behavior.

c. The North American teleconnection

In the case of NA, a warm anomaly exists starting from day 5 and is maximized in the lower troposphere by day 15 as shown in Fig. 3f. Similar to the EA case, dynamic processes are dominant since Fig. 3g shows a very strong low-level warming from day 2 onward, whereas

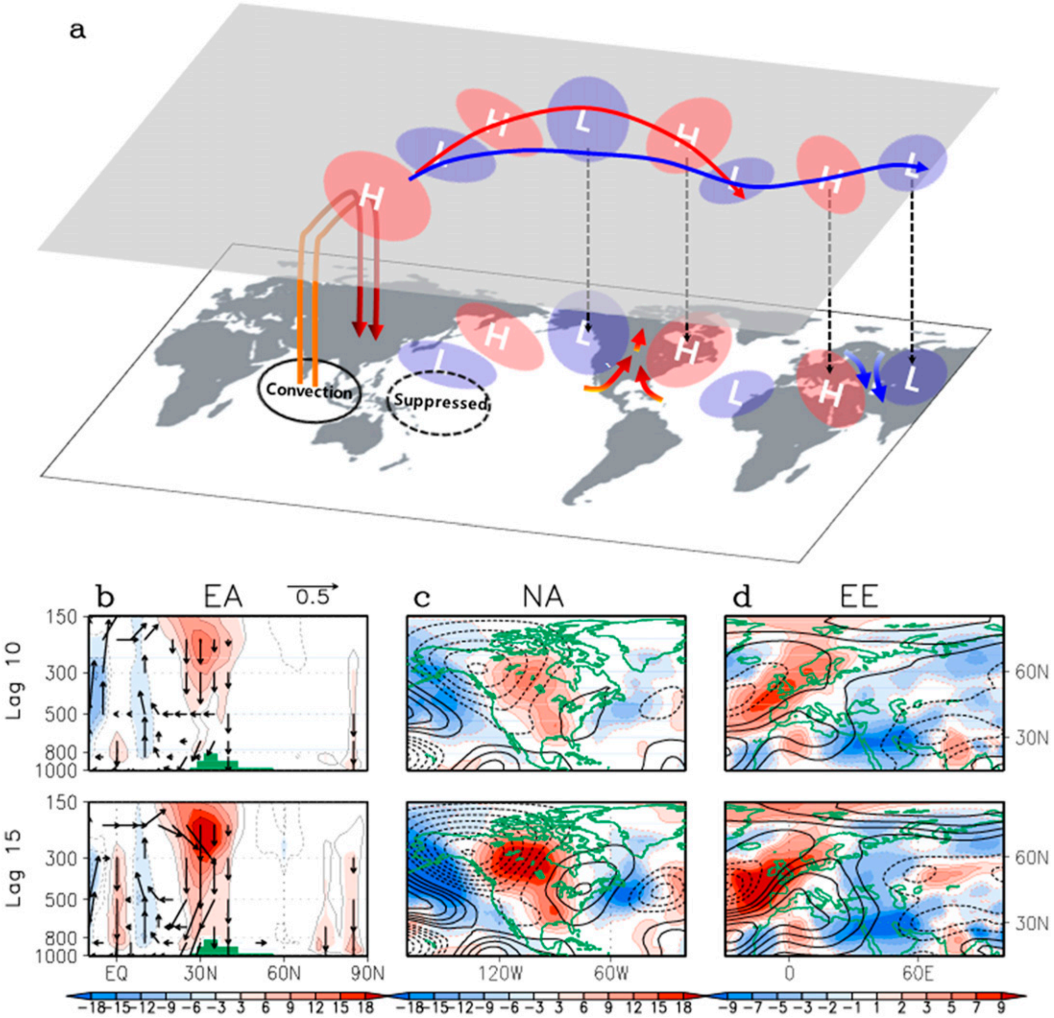

FIG. 5. Hadley circulation and Rossby wave propagation mechanisms of surface temperature change over EA, NA, and EE. (a) Geopotential height anomalies (cyclonic or anticyclonic) are forced by MJO-enhanced convection over the Indian Ocean and suppressed convection over the western Pacific (i.e., phases 1.5–3). The local Hadley circulation is shown as the orange overturning circulation over the Indian Ocean and EA, and subsidence in its downward branch induces adiabatic warming. The Rossby wave activity path for waves reaching NA is denoted as a red line and for waves reaching EE is denoted as a blue line. Warm advection by southerly anomalous winds can be seen in between the cyclonic and anticyclonic anomalies in the lower troposphere over NA, whereas cold advection by northerly anomalies develops over EE. (b) Latitude–height cross section of the lagged composite of air temperature (shading; K) due to adiabatic warming induced by the MJO vertical flow (black arrows) for the initial MJO phase 3. All fields are integrated from lag 0 and the variables are averaged from 60° to 120°E. The magnitude of the reference wind vector (0.5) represents 25 $\mathrm{m\,s^{-1}\,day^{-1}}$ for meridional wind and 0.2 $\mathrm{Pa\,s^{-1}\,day^{-1}}$ for pressure velocity. Shading and vectors represent statistically significant areas at the 95% confidence level. (c) As in (b), but for the air temperature (shading) due to horizontal temperature advection induced by the MJO horizontal flow at 500 hPa for MJO phase 1.5 over NA. Streamfunction anomalies at 500 hPa are denoted as contours (intervals of $15 \times 10^6\ \mathrm{m^2\,s^{-2}\,day^{-1}}$). Integrated warming and cooling regions (shading) are approximately statistically significant at the 90% level. (d) As in (c), but for MJO phase 2 over EE and contour intervals of $8 \times 10^6\ \mathrm{m^2\,s^{-2}\,day^{-1}}$.

diabatic processes (Fig. 3j) show an opposite tendency with a cold anomaly developing at lower levels. A comparison between Figs. 3h and 3i indicates that horizontal temperature advection is dominant among adiabatic processes. The absence of subsidence warming over NA is potentially due to the demise of MJO convection over the Western Hemisphere, so a local Hadley cell cannot develop. Among the advective terms in Eq. (3), horizontal advection of the basic-state temperature field by the MJO-induced horizontal winds is dominant (Fig. 4e). The anomalous temperature advection by the basic-state winds is negative over most of

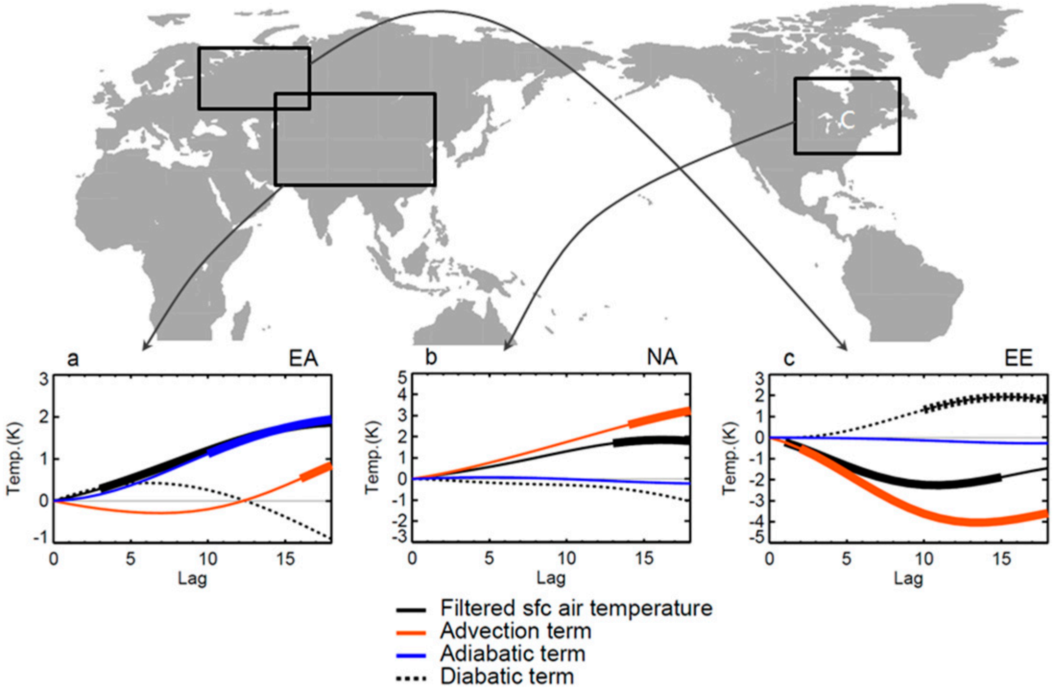

FIG. 6. Time evolution of integrated surface temperature anomalies from tendency, horizontal advective, adiabatic vertical motion, and diabatic terms in Eq. (3). Surface temperature evolution for (a) EA starting at MJO phase 3, (b) NA starting at phase 1.5, and (c) EE starting at phase 2. Values exceeding the 90% confidence level are represented by thick lines.

the troposphere, and the anomaly interaction term is negligible throughout the troposphere.

Warm advection by the MJO-induced horizontal winds can be seen in Fig. 5c, where a cyclonic circulation anomaly centered over Alaska and the northeastern Pacific develops and an anticyclonic circulation anomaly takes place over the eastern part of NA and the Atlantic Ocean. NA is located between the two circulation anomalies so that a southerly flow is formed over this region, causing the warm advection. The MJO-induced circulation is clear evidence of northeastward-propagating Rossby wave activity. The recent severe snowstorm occurred in the winter of 2009/10 showed a similar anomalous pressure distribution with a reversed sign, where strong cold advection by northerlies in between two opposing vorticity anomalies caused the record-breaking heavy snowfall events (Moon et al. 2012).

The time evolution of each term at the surface (see Fig. 6b) illustrates that the magnitude of the advective processes is almost the same as the total dynamic effect, with a fast linear increase until day 15 and a slow increase afterward. Therefore, the MJO effects on the surface warming over these two continents are different. The warming over EA is determined by adiabatic subsidence from the sinking branch of a local Hadley circulation, whereas the warming over NA is due to horizontal warm advection from the MJO-induced southerly flow.

d. The eastern European teleconnection

Another prominent cold anomaly appears over Europe during phases 4 and 5 (Fig. 1). The cold anomaly over EE starts to develop originally during phase 2, when MJO convection is located in the central Indian Ocean (Fig. 2c). At lag 0, a warm anomaly is situated over this area (not shown); however, as time progresses, the warm anomaly weakens and significant cooling occurs. The absolute magnitude of the cold anomaly (~2 K) is as large as those over EA and NA (Fig. 2).

The cooling over EE also comes predominantly from dynamic processes as shown in Fig. 3. It is evident in the vertical structure that horizontal advective processes (Fig. 3m) cause most of the total integrated temperature anomaly (Fig. 3k). The cold anomaly exhibits a peak value at the surface between days 10 and 15 (Fig. 3l). The adiabatic term (Fig. 3n) is negligible, and the diabatic term (Fig. 3o) shows an opposite effect. Therefore, similar to the NA case, horizontal advection tends to control the temperature anomaly strength from the surface up to 300 hPa (see also Fig. 6c) with the northerly wind anomalies induced in between the anticyclonic anomaly over northern Europe and the cyclonic anomaly over EE.

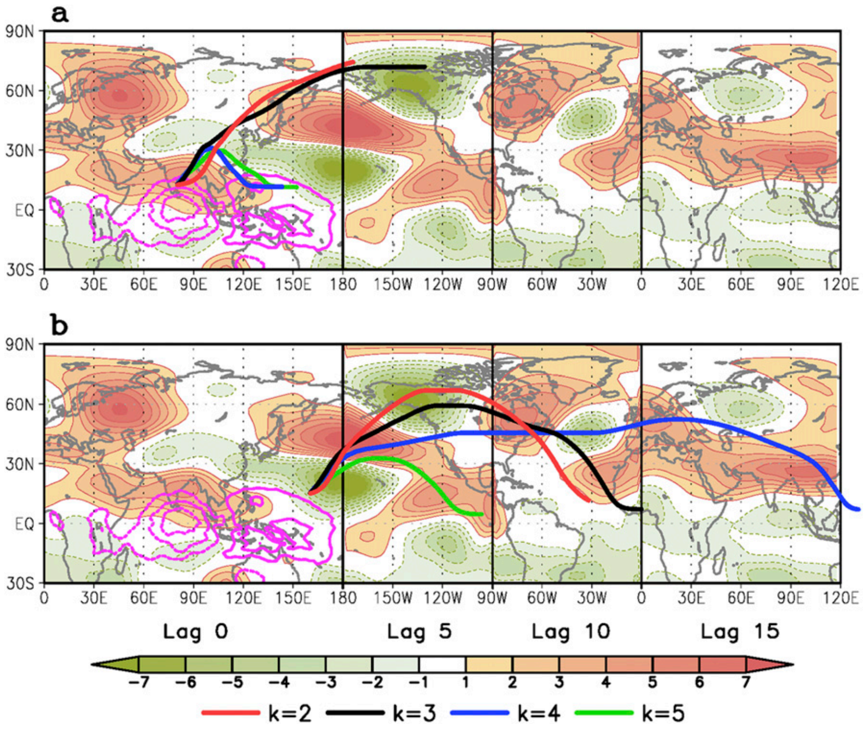

FIG. 7. Rossby wave paths calculated from barotropic Rossby wave theory. The 15-day integrated Rossby wave activity ray for phase 2 forcing is shown for varying k (zonal wavenumber) for (a) enhanced convection over the Indian Ocean and (b) suppressed convection over the western Pacific. The zonal wavenumbers not shown in the figure have a very short or trapped ray in the vicinity of the starting point or critical latitude. The pink contours represent OLR anomalies with a contour interval of 10 W m^{-2}. The lagged composite field of the 300-hPa streamfunction anomaly (contours; interval of 1.0×10^6 m^2 s^{-1}) is presented at (left to right) days 0, 5, 10, and 15 after the initial MJO phase 2. The four lagged composite fields (lags 0–15) are merged into one global streamfunction anomaly field for explicit demonstration of the teleconnection pattern induced by Rossby wave propagation.

The decomposition of the advective term into its three components as shown in Eq. (3) suggests that the basic-state temperature advection due to the MJO-induced horizontal wind anomaly contributes the most (Fig. 4h).

For all these cases, nonlinear interaction in the temperature response to the MJO is negligible so that the extratropical circulation response to the MJO forcing can be interpreted as due to quasi-linear dynamics as stated in Seo and Son (2012).

e. *Physical mechanisms behind the surface temperature variations*

As seen in the above analyses, surface temperature variations over NA and EE are closely related to Rossby wave propagation. To better understand these teleconnections, a ray-tracing method is performed for enhanced convection located over the Indian Ocean.

The Rossby wave ray-tracing result from a 15-day integration of the initial MJO phase 2 (this is used as a representative phase) is presented in Fig. 7, where the upper-troposphere streamfunction anomaly fields are overlaid. The four lagged composite fields are merged into one global streamfunction anomaly field (note that discontinuities are existent since no smoothing is applied) to show a sequential evolution of the streamfunction anomaly as evidence of Rossby wave propagation. For the waves coming from enhanced convection over the Indian Ocean (Fig. 7a), only zonal wavenumbers 2 and 3 survive in reaching the extratropics. The longer wave (zonal wavenumber 2) of the two propagates more slowly and reaches a bit more to the north than the wavenumber-3 wave. The wave activity for the other wavenumbers are trapped or dissipated near the critical latitudes located around the equatorial region; all these are in good agreement with Rossby wave dispersion theory. For the waves emitted from suppressed convection over the western Pacific (Fig. 7b), more waves including zonal wavenumber 4 propagate downstream. Wavenumbers 2 and 3 form a well-known Pacific–North America (PNA)-like teleconnection pattern with a

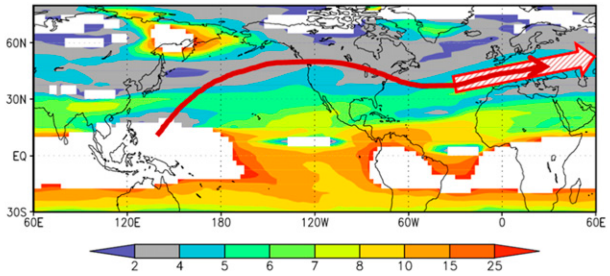

FIG. 8. Stationary total wavenumber K_S field in an asymmetric DJF flow. The stationary wavenumber is calculated by assuming zero zonal phase speed. Shading is presented at wavenumbers 2, 4, 5, 6, 7, 8, 10, 15, and 25. The white region in the tropics indicates singular points in calculating K_S. The red cross-hatched arrow represents a waveguide from the jet stream over the North Atlantic and Europe, and the red thick arrow illustrates the preferred Rossby wave propagation route from the west Pacific.

cyclonic circulation anomaly over Alaska and an anticyclonic circulation anomaly over eastern North America.

Wavenumber 4, whose zonal group velocity is 1.5–3 factors greater than that of wavenumbers 3 and 2 according to the Rossby wave dispersion relationship, tends to affect more downstream regions, crossing the North Atlantic and passing through Europe. Therefore, the surface warming in NA (EE) seen in the previous plots are due to Rossby wave activity from zonal wavenumbers 2 and 3 (4) reaching those areas. A faster wavenumber 4 can reach EE through the eastern Atlantic–Europe waveguide (Hoskins and Ambrizzi 1993) along which the calculated stationary total wavenumber is locally maximized as shown in Fig. 8. This is consistent with Rossby wave theory where the ray tends to refract toward the higher stationary total wavenumber region. Note also that all these waves tend to bend back toward the equator several days later, affecting equatorial circulation and temperature initially affected by equatorially trapped Rossby and Kelvin waves.

Explicit representation of the wave activity propagation path supports the idea that extratropical temperature responses come from Rossby wave dispersion emanating from MJO diabatic heating anomalies. A schematic summarizing these features is presented in Fig. 5a, where two different warming processes (adiabatic subsidence over EA and horizontal temperature advection over NA) are connected to circulation anomalies from a local Hadley circulation and the Rossby wave train forced by anomalous convection in the tropics. The cooling over EE due to Rossby wave propagation coming from the warm pool is also shown.

f. Predictability of strong warm and cold events

A question arises as to how much MJO forcing affects strong temperature events over these continents. We use the total temperature anomaly data rather than the intraseasonally filtered anomaly so not to be subject to real-time bandpass filtering, allowing us to consider a more practically useful diagnostic. A strong warm (cold) temperature event during DJF is defined as a case with a normalized temperature anomaly averaged over EA, NA, and EE being greater (less) than 1.0 (−1.0) standard deviation. This is equivalent to approximately an upper-15th-percentile event. The domain-averaged standard deviation is approximately 4–7 K. The probability of occurrence of extreme events over EA is presented for phase 3 and those over NA for phase 1.5 and over EE for phase 2 (Fig. 9). Over EA, the extreme-event percentage increases until day 20. In particular, the occurrence probability of extreme warming events over central China is more than 40%. The EA-domain-averaged occurrence probability is ~30%. For NA, the probability is smaller than that of EA. However, the probability over the northeastern part of NA amounts to ~30%. On the other hand, Europe experiences cooling at days 10–20. In particular, the cold anomalies develop significantly over eastern and some of northern Europe at day 10. The average probability of the occurrence of a cooling event appears to be 30%. The occurrence probability over these regions for the opposite phase is almost the same.

We have checked the occurrence probability of strong warming or cooling event in the current climate model simulations, which are obtained from the MJO global model comparison project by the Working Group on Numerical Experimentation and the MJO Task Force under the auspices of the Year of Tropical Convection (Moncrieff et al. 2012; Waliser et al. 2012) and the GEWEX Atmospheric System Study. The main results on MJO performance and key physical parameters are reported by Jiang et al. (2015). A previous study of Seo and Wang (2010) suggested that improved MJO simulation (using the NCEP Climate Forecast System models) does improve the global circulation response to the tropical heating.

The composite probability from selected eight good MJO simulation models (Fig. 10, left) shows a generally similar tendency to the observation with the warming over the EA and eastern NA and the cooling over EE. However, as expected, the probability in model is weaker since the circulation response to the tropical forcing is different in different models. The composite maps from six poor MJO simulation models (Fig. 10, right) exhibits no significant signal over the main domains of interest, implying a failure in correctly forecasting extreme temperature events on extended range forecast lead times.

Therefore, a significant portion of the extreme warm/cold events in midlatitudes arise from the direct

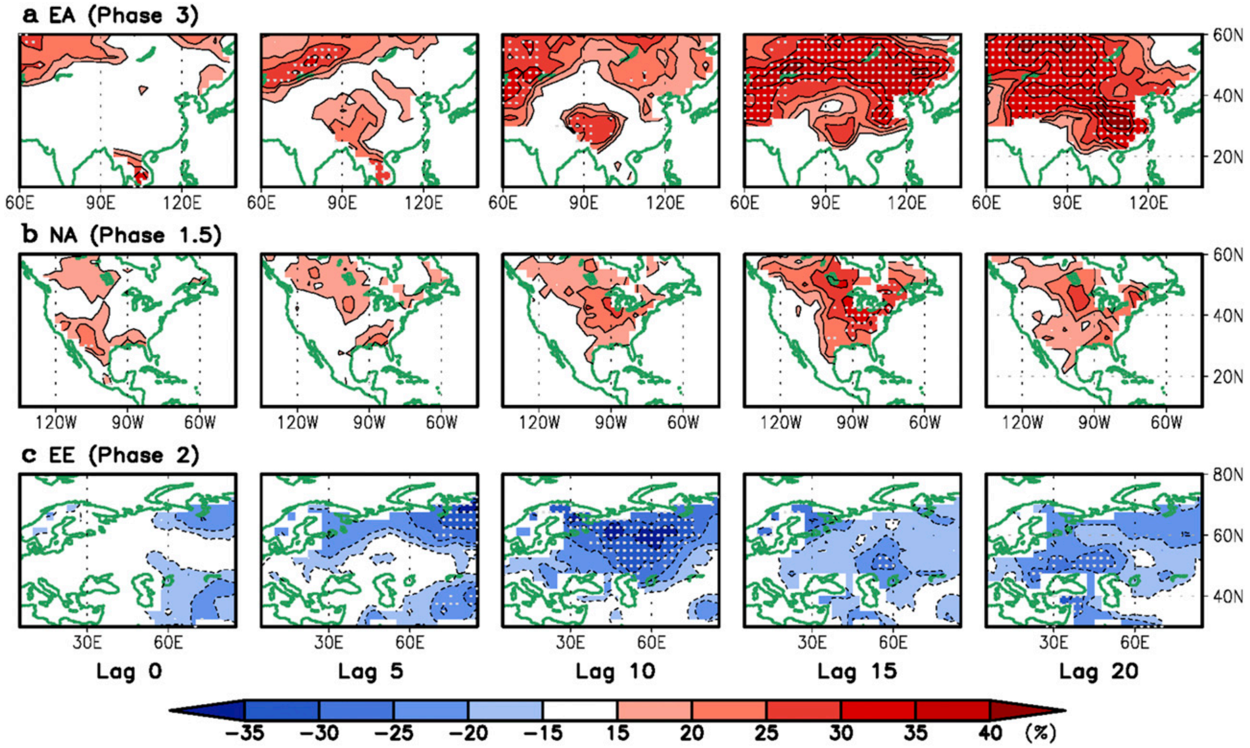

FIG. 9. The percentage of occurrence rates of strong warming events over EA and NA and strong cooling events over EE. Fields are shown at lags 0, 5, 10, 15, and 20 from (a) phase 3 for EA, (b) phase 1.5 for NA, and (c) phase 2 for EE. A strong warming (cooling) event is defined as the case with the normalized temperature greater (less) than 1.0 (−1.0) standard deviation. One standard deviation averaged over each domain is 3.9 K for EA, 6.3 K for NA, and 6.8 K for EE. The dataset used is the HadGHCND gridded station temperature dataset. Dots indicate significant regions at the 95% confidence level.

overturning circulation response and barotropic Rossby wave train propagation induced by MJO heat forcing over the tropics. The information presented in this study is of great importance since it implies that skillful prediction of warm/cold events can be possible with a lead time of about 10–20 days. Furthermore, if one considers that statistical forecast models forecast the MJO skillfully with a lead time of around 15 days (Maharaj and Wheeler 2005; Seo et al. 2009) and that prediction skill of the contemporary atmosphere–ocean coupled forecast systems from ECMWF and NCEP (varEPS and CFSv2) reaches up to 20–30 days (Kim et al. 2014), we may be able to predict strong warm or cold events over extratropical continents as much as 30–45 days ahead, which would be of great utility for society.

Finally, it should also be noted that the MJO is expected to strengthen in a warming climate, by as much as 60%–100% in terms of spectral energy measured by precipitation/OLR or 850-hPa zonal wind variability in MPI's ECHAM5 (Liu et al. 2012) and NCAR's CCSM4 (Subramanian et al. 2014). Consequently, in a future climate, the stronger MJO may be expected to induce teleconnection features containing stronger anomalous circulation fields. This effect alone would cause more frequent occurrences of extreme temperature events such as cold surges, snowstorms and anomalously warm days. Although it requires further study, this may mean that larger variability should be expected to occur in surface air temperature over the northern continents during winter in the future.

4. Summary

We show that a warm or cold event over the NH continents in response to MJO heating is controlled by dynamic processes through overturning meridional circulation and meridionally propagating Rossby waves. For East Asia, a local Hadley circulation arising from the tropical forcing causes adiabatic subsidence following MJO phase 3 (which is the strongest phase during MJO life cycle) to be a main driver for the warming, whereas for North America and eastern Europe, horizontal temperature advection is a key process for inducing the intraseasonal temperature variations. A ray-tracing technique demonstrates that

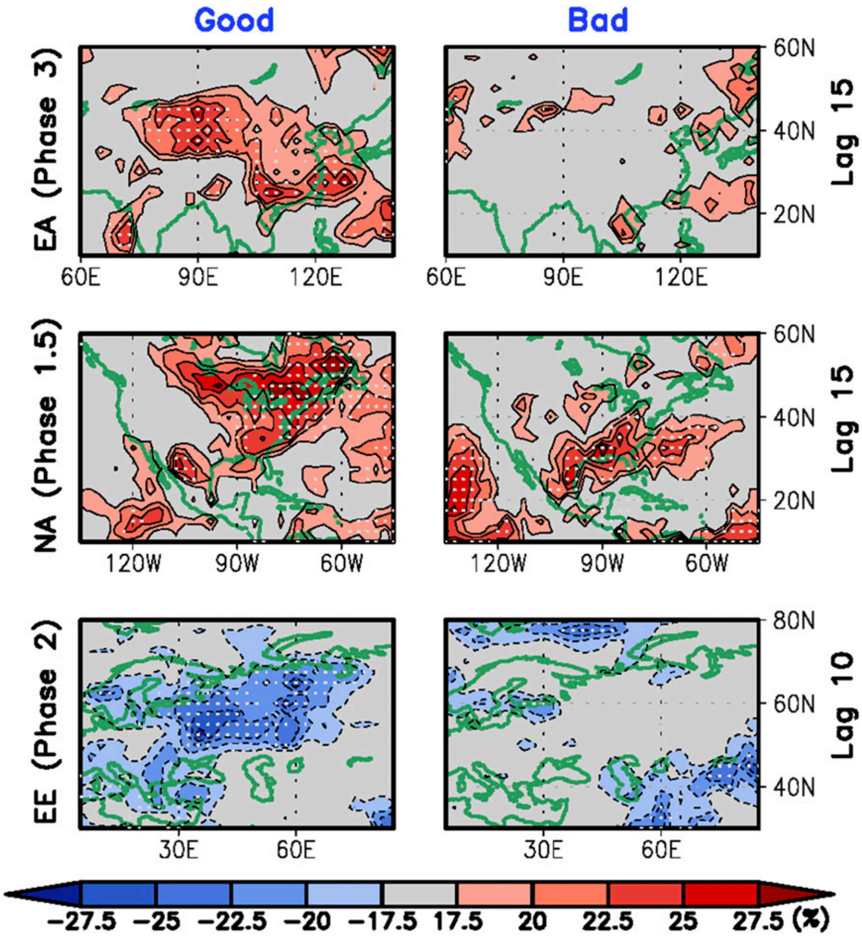

FIG. 10. As in Fig. 9, but for (left) eight good MJO simulation model composite and (right) six bad MJO simulation model composite. (top) Lag days 15 after MJO phase 3 for EA, (middle) lag days 15 after MJO phase 1.5 for NA, and (bottom) lag days 10 after MJO phase 2 for EE.

Rossby waves with zonal wavenumbers 2 and 3 forced by enhanced or suppressed convection over the Indian Ocean and western Pacific influence surface warming over North America, whereas Rossby waves with wavenumber 4 modify surface temperature over eastern Europe. Although recent studies stress the impacts of the Arctic Oscillation, Arctic (Barents and Kara Seas) sea ice melting and Eurasian snow cover variations on extremely cold wintertime episodes over the NH extratropics (Cohen et al. 2014; Kim et al. 2014), extratropical weather and climate for time scales less than a season are considerably affected by tropical heat forcing. It is shown that the MJO is a real potential source of prediction skill for strong warm/cold events over these continents. The current climate models that simulate the MJO realistically demonstrate the spatial distribution of the occurrence probability of extreme temperature events similar to the observed with a weaker magnitude.

Acknowledgments. This work was supported by the National Research Foundation of Korea (NRF) grants funded by the Korea government (MSIP): NRF-2014R1A2A1A11051818 and NRF-2015R1A2A2A01006663. We are very grateful to the three anonymous reviewers for their helpful and constructive comments, which contributed to improving this paper. The authors would like to acknowledge the support from the Korea Institute of Science and Technology Information (KISTI). DMWF was supported by NSF Grants AGS-0846641, AGS-0936059, AGS-1359464, PLR-1341497, and a UW Royalty Research Fund grant.

REFERENCES

Adames, Á. F., and J. M. Wallace, 2014: Three-dimensional structure and evolution of the MJO and its relation to the mean flow. *J. Atmos. Sci.*, **71**, 2007–2026, doi:10.1175/JAS-D-13-0254.1.

Bessafi, M., and M. C. Wheeler, 2006: Modulation of South Indian Ocean tropical cyclones by the Madden–Julian oscillation and convectively coupled equatorial waves. *Mon. Wea. Rev.*, **134**, 638–656, doi:10.1175/MWR3087.1.

Cassou, C., 2008: Intraseasonal interaction between the Madden-Julian oscillation and the North Atlantic Oscillation. *Nature*, **455**, 523–527, doi:10.1038/nature07286.

Cohen, J., and Coauthors, 2014: Recent Arctic amplification and extreme mid-latitude weather. *Nat. Geosci.*, **7**, 627–637, doi:10.1038/ngeo2234.

Hall, J., A. Matthews, and D. Karoly, 2001: The modulation of tropical cyclone activity in the Australian region by the Madden–Julian oscillation. *Mon. Wea. Rev.*, **129**, 2970–2982, doi:10.1175/1520-0493(2001)129<2970:TMOTCA>2.0.CO;2.

Hendon, H. H., and B. Liebmann, 1990: The intraseasonal (30–50 day) oscillation of the Australian summer monsoon. *J. Atmos. Sci.*, **47**, 2909–2923, doi:10.1175/1520-0469(1990)047<2909:TIDOOT>2.0.CO;2.

Ho, C.-H., J.-H. Kim, J.-H. Jeong, H.-S. Kim, and D. Chen, 2006: Variation of tropical cyclone activity in the South Indian Ocean: El Niño–Southern Oscillation and Madden-Julian Oscillation effects. *J. Geophys. Res.*, **111**, D22101, doi:10.1029/2006JD007289.

Hoskins, B. J., and D. J. Karoly, 1981: The steady linear response of a spherical atmosphere in thermal and orographic forcing. *J. Atmos. Sci.*, **38**, 1179–1196, doi:10.1175/1520-0469(1981)038<1179:TSLROA>2.0.CO;2.

——, and T. Ambrizzi, 1993: Rossby wave propagation on a realistic longitudinally varying flow. *J. Atmos. Sci.*, **50**, 1661–1671, doi:10.1175/1520-0469(1993)050<1661:RWPOAR>2.0.CO;2.

Hoyos, C. D., and P. J. Webster, 2007: The role of intraseasonal variability in the nature of Asian monsoon precipitation. *J. Climate*, **20**, 4402–4424, doi:10.1175/JCLI4252.1.

Jeong, J.-H., C.-H. Ho, B.-M. Kim, and W.-T. Kwon, 2005: Influence of the Madden-Julian Oscillation on wintertime surface air temperature and cold surges in east Asia. *J. Geophys. Res.*, **110**, D11104, doi:10.1029/2004JD005408.

Jiang, X., and Coauthors, 2015: Vertical structure and physical processes of the Madden-Julian oscillation: Exploring key model physics in climate simulations. *J. Geophys. Res. Atmos.*, **120**, 4718–4748, doi:10.1002/2014JD022375.

Jin, F., and B. J. Hoskins, 1995: The direct response to tropical heating in a baroclinic atmosphere. *J. Atmos. Sci.*, **52**, 307–319, doi:10.1175/1520-0469(1995)052<0307:TDRTTH>2.0.CO;2.

Kerr, R. A., 2006: Rivers in the sky are flooding the world with tropical waters. *Science*, **313**, 5786, doi:10.1126/science.313.5786.435.

Kim, B.-M., S.-W. Son, S.-K. Min, J.-H. Jeong, S.-J. Kim, X.-D. Zhang, T. Shim, and J.-H. Yoon, 2014: Weakening of the stratospheric polar vortex by Arctic sea-ice loss. *Nat. Commun.*, **5**, 4646, doi:10.1038/ncomms5646.

L'Heureux, M. L., and R. W. Higgins, 2008: Boreal winter links between the Madden–Julian oscillation and the Arctic Oscillation. *J. Climate*, **21**, 3040–3050, doi:10.1175/2007JCLI1955.1.

Liebmann, B., H. H. Hendon, and J. D. Glick, 1994: The relationship between tropical cyclones of the western Pacific and Indian Oceans and the Madden-Julian Oscillation. *J. Meteor. Soc. Japan*, **72**, 401–411.

Lin, H., and G. Brunet, 2009: The influence of the Madden–Julian oscillation on Canadian wintertime surface air temperature. *Mon. Wea. Rev.*, **137**, 2250–2262, doi:10.1175/2009MWR2831.1.

——, ——, and J. Derome, 2009: An observed connection between the North Atlantic Oscillation and the Madden–Julian oscillation. *J. Climate*, **22**, 364–380, doi:10.1175/2008JCLI2515.1.

Liu, P., T. Li, B. Wang, M. Zhang, J.-J. Luo, Y. Masumoto, X. Wang, and E. Roeckner, 2012: MJO change with A1B global warming estimated by the 40-km ECHAM5. *Climate Dyn.*, **41**, 1009–1023, doi:10.1007/s00382-012-1532-8.

Madden, R. A., and P. R. Julian, 1972: Description of global-scale circulation cells in the tropics with a 40–50 day period. *J. Atmos. Sci.*, **29**, 1109–1123, doi:10.1175/1520-0469(1972)029<1109:DOGSCC>2.0.CO;2.

Maharaj, E. A., and M. C. Wheeler, 2005: Forecasting an index of the Madden-Julian oscillation. *Int. J. Climatol.*, **25**, 1611–1618, doi:10.1002/joc.1206.

Maloney, E. D., and J. Shaman, 2008: Intraseasonal variability of the West Africa monsoon and Atlantic ITCZ. *J. Climate*, **21**, 2898–2918, doi:10.1175/2007JCLI1999.1.

Matthews, A. J., B. J. Hoskins, and M. Masutani, 2004: The global response to tropical heating in the Madden–Julian oscillation during the northern winter. *Quart. J. Roy. Meteor. Soc.*, **130**, 1991–2011, doi:10.1256/qj.02.123.

McPhaden, M. J., 1999: Genesis and evolution of the 1997-98 El Niño. *Science*, **283**, 950–954, doi:10.1126/science.283.5404.950.

Moncrieff, M. W., D. E. Waliser, M. J. Miller, M. A. Shapiro, G. R. Asrar, and J. Caughey, 2012: Multiscale convective organization and the YOTC virtual global field campaign. *Bull. Amer. Meteor. Soc.*, **93**, 1171–1187, doi:10.1175/BAMS-D-11-00233.1.

Moon, J.-Y., B. Wang, and K.-J. Ha, 2012: MJO modulation on 2009/10 winter snowstorms in the United States. *J. Climate*, **25**, 978–991, doi:10.1175/JCLI-D-11-00033.1.

Oliver, E. C. J., 2015: Multidecadal variations in the modulation of Alaska wintertime air temperature by the Madden–Julian Oscillation. *Theor. Appl. Climatol.*, **121**, 1–11, doi:10.1007/s00704-014-1215-y.

Press, W. H., S. A. Teukolsky, W. Y. Vetterling, and B. P. Flannery, 1992: *Numerical Recipes in Fortran 77: The Art of Scientific Computing*. Cambridge University Press, 931 pp.

Riddle, E. E., M. B. Stoner, N. C. Johnson, M. L. L'Heureux, D. C. Collins, and S. B. Feldstein, 2013: The impact of the MJO on clusters of wintertime circulation anomalies over the North American region. *Climate Dyn.*, **40**, 1749–1766, doi:10.1007/s00382-012-1493-y.

Seo, K.-H., and W. Wang, 2010: The Madden–Julian oscillation simulated in the NCEP Climate Forecast System model: The importance of stratiform heating. *J. Climate*, **23**, 4770–4793, doi:10.1175/2010JCLI2983.1.

——, and S.-W. Son, 2012: The global atmospheric circulation response to tropical diabatic heating associated with the Madden–Julian oscillation during northern winter. *J. Atmos. Sci.*, **69**, 79–96, doi:10.1175/2011JAS3686.1.

——, J.-K. E. Schemm, W. Wang, and A. Kumar, 2007: The boreal summer intraseasonal oscillation simulated in the NCEP Climate Forecast System (CFS): The effect of sea surface temperature. *Mon. Wea. Rev.*, **135**, 1807–1827, doi:10.1175/MWR3369.1.

——, W. Wang, J. Gottschalck, Q. Zhang, J.-K. E. Schemm, W. R. Higgins, and A. Kumar, 2009: Evaluation of MJO forecast skill from several statistical and dynamical forecast models. *J. Climate*, **22**, 2372–2388, doi:10.1175/2008JCLI2421.1.

Sobel, A. H., and E. D. Maloney, 2000: Effect of ENSO and the MJO on western North Pacific tropical cyclones. *Geophys. Res. Lett.*, **27**, 1739–1742, doi:10.1029/1999GL011043.

Subramanian, A., M. Jochum, A. J. Miller, R. Neale, H. Seo, D. Waliser, and R. Murtugudde, 2014: The MJO and global warming: A study in CCSM4. *Climate Dyn.*, **42**, 2019–2031, doi:10.1007/s00382-013-1846-1.

Vecchi, G. A., and N. A. Bond, 2004: The Madden-Julian Oscillation (MJO) and northern high-latitude wintertime surface air temperatures. *Geophys. Res. Lett.*, **31**, L04104, doi:10.1029/2003GL018645.

Waliser, D. E., and Coauthors, 2012: The ''Year'' of Tropical Convection (May 2008–April 2010): Climate variability and weather highlights. *Bull. Amer. Meteor. Soc.*, **93**, 1189–1218, doi:10.1175/2011BAMS3095.1.

Wheeler, M. C., and H. H. Hendon, 2004: An all-season real-time multivariate MJO index: Development of an index for monitoring and prediction. *Mon. Wea. Rev.*, **132**, 1917–1932, doi:10.1175/1520-0493(2004)132<1917:AARMMI>2.0.CO;2.

——, and J. L. McBride, 2005: Australian-Indonesian monsoon. *Intraseasonal Variability in the Atmosphere-Ocean Climate System*, W. Lau and D. Waliser, Eds., Springer Praxis, 125–173.

Yanai, M., S. Esbensen, and J.-H. Chu, 1973: Determination of bulk properties of tropical cloud clusters from large-scale heat and moisture budgets. *J. Atmos. Sci.*, **30**, 611–627, doi:10.1175/1520-0469(1973)030<0611:DOBPOT>2.0.CO;2.

Yasunari, T., 1979: Cloudiness fluctuations associated with the Northern Hemisphere summer monsoon. *J. Meteor. Soc. Japan*, **57**, 227–242.

Yoo, C., S. Lee, and S. Feldstein, 2012a: Mechanisms of Arctic surface air temperature change in response to the Madden–Julian oscillation. *J. Climate*, **25**, 5777–5790, doi:10.1175/JCLI-D-11-00566.1.

——, ——, and ——, 2012b: Arctic response to an MJO-like tropical heating in an idealized GCM. *J. Atmos. Sci.*, **69**, 2379–2393, doi:10.1175/JAS-D-11-0261.1.

Zavala-Garay, J., C. Zhang, A. Moore, and R. Kleeman, 2005: The linear response of ENSO to the Madden–Julian oscillation. *J. Climate*, **18**, 2441–2459, doi:10.1175/JCLI3408.1.

Zhou, S., and A. J. Miller, 2005: The interaction of the Madden–Julian oscillation and the Arctic Oscillation. *J. Climate*, **18**, 143–159, doi:10.1175/JCLI3251.1.

Zhou, Y., K. Thompson, and Y. Lu, 2011: Mapping and understanding the relationship between Northern Hemisphere winter surface temperature and the Madden–Julian oscillation. *Mon. Wea. Rev.*, **139**, 2439–2445, doi:10.1175/2011MWR3587.1.